Novel multi-heterostructured Pt-BiOBr/TiO_2 nanotube arrays with remarkable visible-light photocatalytic performance and stability*

LIU Jia-qin (刘家琴)[1,2,3]**, **DAI Meng-jia** (戴梦嘉)[1], **RUAN Li-li** (阮丽丽)[4], **XU Juan** (徐娟)[5], **WANG Yan** (王岩)[4], **and WU Yu-cheng** (吴玉程)[2,3]

1. Institute of Industry & Equipment Technology, Hefei University of Technology, Hefei 230009, China

2. Anhui Provincial Key Laboratory of Advanced Functional Materials and Devices, Hefei 230009, China

3. Department of Electronic Materials Engineering, Australian National University, Canberra 2601, Australia

4. School of Materials Science and Engineering, Hefei University of Technology, Hefei 230009, China

5. School of Chemistry and Chemical Engineering, Hefei University of Technology, Hefei 230009, China

(Received 8 February 2017; Revised 2 March 2017)

Unique multiple heterojunction of Pt-BiOBr/TiO_2 nanotube arrays (Pt-BiOBr/TNTAs) was achived by successively loading both Pt nanoparticles (NPs) and BiOBr nanoflkes (NFs) on surface of ordered and spaced TiO_2 nanotubes (NTs) using anodization followed by solvothermal and sequential chemical bath deposition (S-CBD) method. The fabricated Pt-BiOBr/TNTAs were fully characterized, and the photocatalytic (PC) activity and stability of Pt-BiOBr/TNTAs toward degradation of methyl orange (MO) under visible-light irradiation (λ>400 nm) were evaluated. The results reveal that multiple heterostructures of Pt/TiO_2, Pt/BiOBr and BiOBr/TiO_2 are constructed among TNTAs substrate, Pt NPs and BiOBr NFs, and the hybrid Pt-BiOBr/TNTAs catalyst exhibits remarkable visible-light PC activity, favourable reusability and long-term stability. The combined effect of several factors may contribute to the remarkable PC performance, including strong visible-light absorption by both Pt NPs and BiOBr NFs, lower recombination rate of photo-generated electrons and holes attributed to the multiple heterojunction, microstructures for facile light injection and adsorption as well as efficient mass transport, and larger specific surface area for enhancing light absorption, increasing the effective contact area between the absorbed dye molecules and catalyst and benefiting the molecule transport of reactants or products.

Document code: A **Article ID:** 1673-1905(2017)03-0165-7

DOI 10.1007/s11801-017-7023-8

With increasing concerns over environment problems and global energy crisis, utilizing solar energy as the driving force for semiconductors to degrade pollutants into nontoxic materials is critical to the continuation of socio-economic development. Among all photocatalytic (PC) materials, TiO_2 remains one of the most promising catalysts because it is photostable, low-cost, nontoxic and high photoactive. Among various TiO_2 materials with different geometrical shapes and microstructures, TiO_2 nanotube arrays (TNTAs) has proven to be an outstanding photocatalyst due to the ordered porous architecture, large surface area, long charge carrier lifetime and simple fabrication[1-3]. Moreover, TNTAs may serve as a good support for versatile photoactive materials to form hybrid systems.

Nevertheless, the intrinsic wide band gap of TiO_2 (3.2 eV for anatase and 3.0 eV for rutile) limits its absorption in the ultraviolet (UV) region of solar spectrum. Moreover, rapid electrons-holes recombination greatly lowers the quantum efficiency of TNTAs. Therefore, numerous attempts[3,4] have been dedicated to improve the quantum yield and efficiency of TNTAs, including anion doping, metal ion-implantation, heterojunction construction with narrow-gap semiconductors, surface modification with noble metal and surface sensitization.

BiOX (X=Cl, Br, I) has become a new promising photocatalyst since Zhang et al[5] first reported that nanostructured BiOCl has higher PC performance than commercial TiO_2 (P25). The strong internal static electric fields and the unique layered structure enable the effective electron-hole separation, assisting high PC performance of BiOX[6,7]. In our previous work, a series of

* This work has been supported by the National Natural Science Foundation of China (Nos.51402078 and 51302060), Anhui Provincial Natural Science Foundation (No.1408085QE85), and the Young Scholar Enhancement Foundation (Plan B) of Hefei University of Technology in China (No.JZ2016HGTB0711).

** E-mail: jqliu@hfut.edu.cn

heterostructured BiOI/TNTAs[8] and BiOBr/TNTAs[9] catalysts were successfully achieved using anodization followed by the sequential chemical bath deposition (S-CBD) method, and they showed outstanding visible-light photoelectrocatalytic and PC activities toward degradation of organic pollutants.

Herein, a novel multi-heterostructured Pt-BiOBr/TNTAs catalyst was firstly achieved by successively loading both Pt nanoparticles (NPs) and BiOBr nanoflkes (NFs) on surface of ordered and spaced TiO_2 nanotubes (NTs) using anodization followed by solvothermal and S-CBD method, and the as-fabricated Pt-BiOBr/TNTAs catalyst exhibits remarkable visible-light PC activity and favourable stability towards the degradation of organic pollutants, which can far outperform those of our previously reported BiOBr/TNTAs catalyst.

Ordered and spaced TNTAs were fabricated by anodization of titanium (Ti) foils (2.0 cm×2.5 cm, 99.7%) in a 0.25 mol/L NH_4F ethylene glycol (EG) solution containing 8% water (volume percentage). Anodization was performed on a two-electrode setup connected to a direct current (DC) power supply with Ti foil and graphite foil as the working and counter electrodes respectively at a constant voltage of 60 V for 4 h. Prior to anodization, Ti foils were ultrasonically cleaned in acetone, ethanol and deionized water, successively. After anodization, the as-fabricated amorphous TNTAs were annealed at 500 °C for 2 h with a heating rate of 2 °C·min^{-1}.

Pt/TNTAs were prepared by solvothermal technique. 10 mL 2 mmol/L chloroplatinic acid (H_2PtCl_6) ethanol solution containing 6 mmol/L citric acid ($C_6H_8O_7$) and 1 mL ultrapure water was first poured into a Φ25 mm×25 mm weighing bottle. Then immerse the TNTAs into above bottle, put the bottle into the autoclave with a teflon tank, and add right amount of water into the autoclave. Subsequently the autoclave was heated at 100 °C for 10 h.

Pt-BiOBr/TNTAs were fabricated via the S-CBD method. 1 mmol $Bi(NO_3)_3·5H_2O$ was dissolved in 20 mL 0.1 mol/L mannitol solution to obtain solution A, and 1 mmol NaBr was dissolved in 20 mL ultrapure water to obtain solution B. Then, these two solutions were placed into the 40°C water bath. Pt/TNTAs were first immersed in solution A for 2 min and rinsed with absolute ethanol, and then immersed in solution B for 2 min and rinsed with absolute ethanol again. Such a reaction cycle was repeated twice. For comparison, above process was applied to bare TNTAs, and the resulting sample was marked as BiOBr/TNTAs.

Morphologies of as-prepared samples were observed using SU8020 field-emission scanning electron microscopy (FESEM) operated at 5.0 kV and JEM-2100F high resolution transmission electronic microscopy (HRTEM) operated at 200 kV. Phase structures were identified by X-ray diffraction (XRD) analysis on a Rigaku D/Max-2500 V diffractometer. The chemical constituents were investigated by X-ray photoelectron spectroscopy (XPS) on the ESCALAB250Xi measuring system with Mg Kα X-ray source. UV-vis diffuse reflectance spectrum (DRS) was measured on a Shimadzu UV 3600 UV-vis-NIR spectrophotometer using $BaSO_4$ as a reference. Nitrogen adsorption isotherms were conducted at 77.15 K on a micromeritics analyzer (SA3100) after degassing the samples at 373.15 K for 2 h. The Brunauer-Emmett-Teller (BET) surface area was estimated in a relative pressure range from 0.05 to 0.2.

PC activity of the as-prepared samples was evaluated based on PC degradation of methyl orange (MO) solution under visible-light irradiation using a XPA-7 photochemical reactor (Nanjing Xujiang Machine-electronic Plant, China). The schematic diagram of the PC activity evaluation setup is shown in Fig.1. A 250 W metal halogen lamp with a 400 nm UV-cut filter was utilized as visible-light source with the illumination intensity of 174 mW/cm^2. Distance between the lamp and the test-tube was kept at 10 cm. Before light irradiation, the fabricated 2.0 cm×2.5 cm samples were immersed in 15 mL MO solution (10 mg·L^{-1}) for 1 h to establish adsorption-desorption equilibrium. Upon light irradiation, the MO solution was sampled every 30 min to monitor the concentration variation using a Shimadzu UV3600 spectrophotometer by recording the variation of the absorption peak at λ=464 nm. The removal rate R (%) can be calculated by[10]

$$R=[(C_0-C)/C_0]\times 100\%=(A_0-A)/A_0, \quad (1)$$

where C_0 and C are the initial and real-time concentration of MO solution, and A_0 and A are the initial and real-time absorbance at 464 nm.

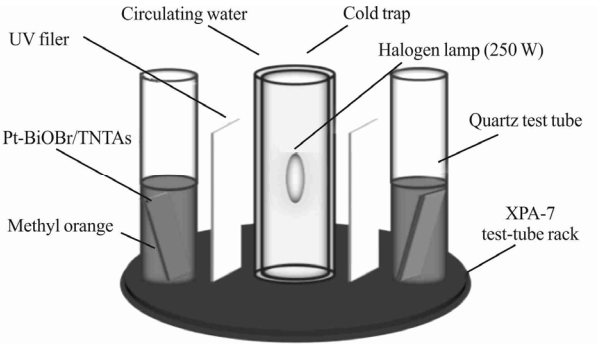

Fig.1 Schematic diagram of the PC activity evaluation setup tested by the XPA-7 photochemical reactor

The XRD patterns shown in Fig.2 present the phase structure and crystallinity of as-fabricated samples. For bare TNTAs, all diffraction peaks can be well indexed to anatase TiO_2 phase (JCPDS No.21-1272) except for the Ti peaks, which demonstrates that amorphous structure transforms to anatase TiO_2 under thermal treatment. For Pt/TNTAs, all diffraction peaks are nearly the same with those of bare TNTAs. No typical peak of Pt can be observed, which should be ascribed to low loading amount of Pt and peak broadening caused by nano-sized Pt NPs.

In contrast with patterns of bare TNTAs and Pt/TNTAs, diffraction peaks of BiOBr emerge in patterns of both BiOBr/TNTAs and Pt-BiOBr/TNTAs at around 10.5°, 32.4° and 46.2°, which can be indexed to (001), (110) and (200) planes of tetragonal BiOBr.

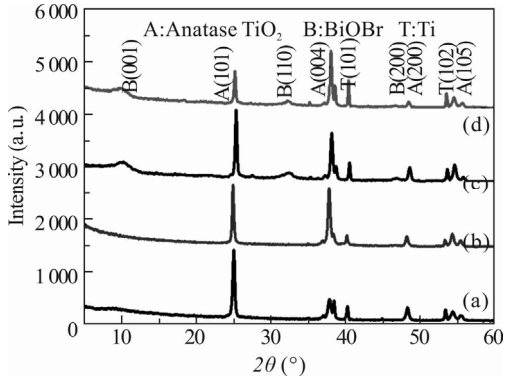

Fig.2 XRD patterns of (a) bare TNTAs, (b) Pt/TNTAs, (c) BiOBr/TNTAs and (d) Pt-BiOBr/TNTAs

Morphologies of the as-prepared samples directly observed by FESEM are shown in Fig.3. It is clear in Fig.3(a) that bare TNTAs are composed of vertically oriented, highly-ordered and round-like NTs with length of about 20 μm, average inner diameter of about 150 nm and wall thickness of 20—25 nm. The obvious difference to the conventional TNTAs is that the NTs are free-standing and well-separated from each other with inter-tube spacing ranging from 8 nm to 20 nm. The free space between tubes allows more exposed surface for the deposition of a secondary material as well as efficient mass transport. For Pt/TNTAs shown in Fig.3(b), both the outer and inner walls of TiO_2NTs are fully and uniformly coated by large amount of Pt NPs with diameter of only several nanometers. There is no apparent decrease in the effective intertube spacing and tube diameter, which means that all microstructures of Pt/TNTAs are still facile for the subsequent deposition of BiOBr. After BiOBr deposition, as shown in Fig.3(c), large amounts of NFs are loaded on both outer and inner walls of TiO_2 NTs apart from previously deposited NPs. These NFs are only several nanometers in thickness and 20—30 nm in width. Moreover, these NFs prefer to grow by attaching the tube-walls or previously deposited NPs, and consequently multiple heterojunctions of Pt/TiO_2, Pt/BiOBr and BiOBr/TiO_2 can be successfully constructed in the Pt-BiOBr/TNTAs hybrid. It is obvious that TiO_2 NTs maintain the hollow structure without mouth blocking, and intertube spacings still remain interconnecting. Large amounts of ultrafine NPs and NFs help to increase the specific surface area and effective contact area between the catalyst and the degraded molecules, as well as enhance the effective light absorption due to the multi-reflections among Pt NPs, BiOBr NFs and TiO_2 NTs[8]. In short, all microstructures of Pt-BiOBr/TNTAs are beneficial to the subsequent degradation reaction. In addition, Fig.3(d) shows the morphology of BiOBr/TNTAs prepared for comparison. A large number of BiOBr NFs are fully loaded onto both outer and inner walls of TiO_2 NTs.

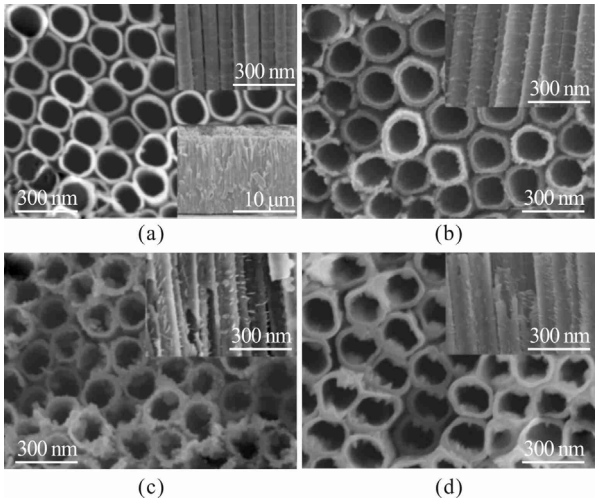

Fig.3 FESEM images of (a) bare TNTAs, (b) Pt/TNTAs, (c) Pt-BiOBr/TNTAs and (d) BiOBr/TNTAs

Structure characteristics and the presence of heterostructures for both Pt/TNTAs and Pt-BiOBr/TNTAs were further analyzed using HRTEM, as illustrated in Fig.4. For Pt/TNTAs shown in Fig.4(a) and (b), Pt NPs with diameter of 6—8 nm distribute uniformly over the whole tube-walls. The corresponding HRTEM image in Fig.4(b) further confirms the existence of Pt/TiO_2 heterotructure. The spherical part with lattice space of 0.199 nm corresponds to Pt (200) plane, and the rest part with lattice space of 0.243 nm corresponds to TiO_2 (103) plane. TEM image for Pt-BiOBr/TNTAs shown in Fig.4(c) also confirms former FESEM result that both the outer and inner walls of TiO_2 NTs were densely coated with large number of Pt NPs as well as BiOBr NFs. Both Pt NPs and BiOBr NFs are ultrafine and darker than TiO_2 NTs. Multiple heterostructures can be directly observed from the HRTEM image of the selected areas marked with blocks in Fig.4(c). As shown in Fig.4(d), several neighbouring lattice parts with lattice space of 0.242 nm, 0.811 nm and 0.227 nm correspond to (103) planes of anatase TiO_2, (111) plane of tetragonal BiOBr and (111) plane of Pt, respectively. Moreover, well-defined lattice fringes reveal the good crystallinity of the materials. The layered structure of BiOBr can also be clearly observed. Therefore, HRTEM analysis for Pt-BiOBr/TNTAs certainly demonstrates that multi-heterostructures of Pt/TiO_2, Pt/BiOBr and BiOBr/TiO_2 are successfully constructed among TNTAs substrate, deposited Pt NPs and BiOBr NFs.

Surface composition and chemical state were further characterized by XPS. XPS spectra of Pt/TNTAs and Pt-BiOBr/TNTAs are illustrated in Figs.5 and 6. The XPS spectrum of Pt/TNTAs in Fig.5(a) shows that it primarily

contains 4 elements of Ti, O, C and Pt. The XPS peak for C 1s at 284.7 eV is ascribed to the CO_2 absorbed on the sample surface from air or adventitious hydrocarbon in the XPS instrument. In the high resolution XPS spectrum of Ti 2p shown in Fig.5(b), two distinct peaks at around 458.8 eV and 464.7 eV are consistent with the characteristic Ti $2p_{1/2}$ and Ti $2p_{3/2}$ of Ti^{4+} in anatase TiO_2[11,12]. The O 1s core level spectrum shown in Fig.5(c) can be fitted into two peaks, corresponding to the Ti-O (530.3 eV) of TiO_2[11-13] and the hydroxyl group (531.7 eV)[13]. The high-resolution spectrum of Pt 4f in Fig.5(d) shows two intense peaks at around 70.8 eV and 73.9 eV, respectively, which are attributed to Pt $4f_{7/2}$ and Pt $4f_{5/2}$ excitation of metallic Pt[14]. XPS analysis for Pt/TNTAs confirms that Pt, Ti and O elements exist in the form of metallic Pt and anatase TiO_2.

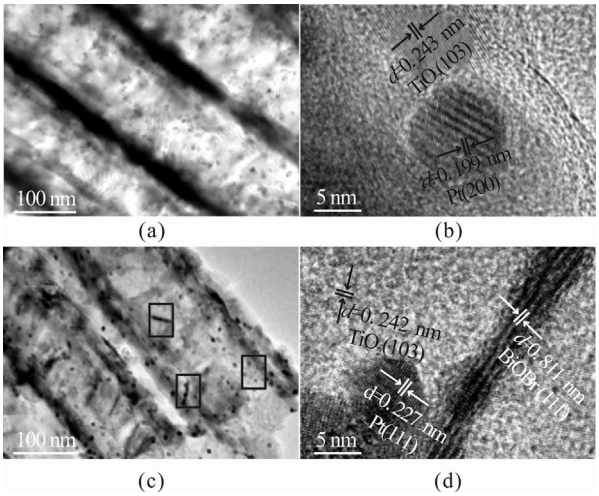

Fig.4 TEM images and HRTEM images of (a, b) Pt/TNTAs and (c, d) Pt-BiOBr/TNTAs

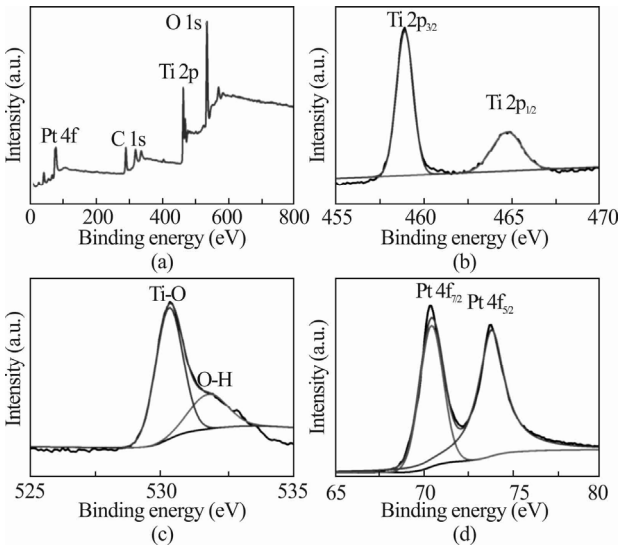

Fig.5 (a) XPS spectrum of Pt/TNTAs and high resolution XPS spectra around (b) Ti 2p, (c) O 1s and (d) Pt 4f peaks

As shown in Fig.6(a), Bi and Br elements emerge in the Pt-BiOBr/TNTAs XPS spectrum in addition to Ti, O, C and Pt elements. In Bi 4f spectrum shown in Fig.6(b), two peaks centered at 159.1 eV and 164.5 eV are assigned to Bi $4f_{7/2}$ and Bi $4f_{5/2}$, respectively, which are characteristic peaks of Bi^{3+} in BiOBr[15]. For O 1s core level spectrum shown in Fig.6(c), three distinct peaks are clearly observed at 529.4 eV, 530.0 eV and 531.2 eV, which correspond to the Bi-O in $[Bi_2O_2]$ slabs of BiOBr layered structure[9,15], Ti-O of TiO_2[11-13] and the hydroxyl group[13], respectively. High resolution spectrum of both Br 3d and Pt 4f in Fig.6(d) clearly show that the binding energy of Br 3d is very close to that of Pt 4f. Two peaks at 68.4 eV and 69.3 eV in Br 3d spectrum (inset I) corresponds to Br $3d_{5/2}$ and Br $3d_{3/2}$, which are ascribed to Br^- in BiOBr[9,15]. Two peaks at 71.1 eV and 74.4 eV in Pt 4f spectrum (inset II) are assigned to Pt $4f_{7/2}$ and Pt $4f_{5/2}$, which are consistent with previous XPS result of Pt element in Pt/TNTAs. As a consequence, XPS analysis for Pt-BiOBr/TNTAs again confirms the coexistence of both Pt and BiOBr deposit and TiO_2 substrate.

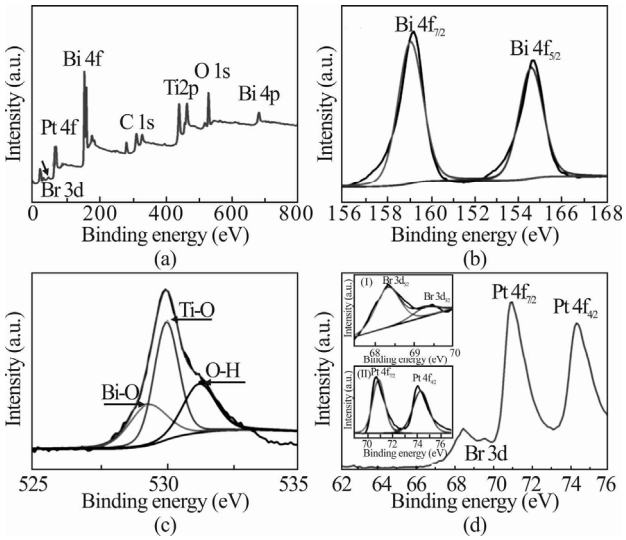

Fig.6 (a) XPS spectrum of Pt-BiOBr/TNTAs and high resolution XPS spectra around (b) Bi 4f, (c) O 1s, (d) Br 3d (inset I) and Pt 4f (inset II) peaks

Fig.7 shows the UV-vis DRS of the tested samples. It is clear that the bare TNTAs are only active in UV light region, which is ascribed to the intrinsic band gap absorption of TiO_2. Pt/TNTAs show obvious visible-light absorption, which can be attributed to the localized surface plasmon resonance (LSPR) of the loading Pt NPs[16,17], further confirming the successful deposition of Pt NPs. For BiOBr/TNTAs, the light absorption is broadened to visible-light region, and the absorption edge is located at around 425 nm. Compared with both Pt/TNTAs and BiOBr/TNTAs, visible-light absorption of Pt-BiOBr/TNTAs is further enhanced, and the absorption edge shows a certain red-shift, which may probably due to the synergetic effect of visible-light absorption from

BiOBr and Pt, multi-heterojunctions, higher specific area, as well as the mircostructures.

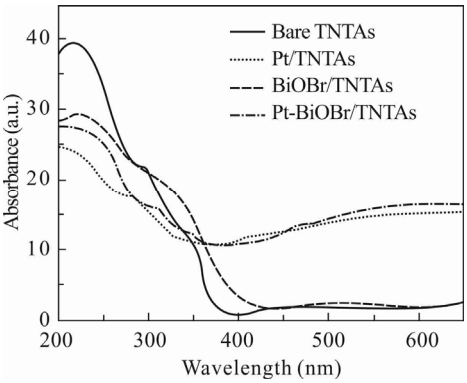

Fig.7 UV-vis DRS of bare TNTAs, Pt/TNTAs, BiOBr/TNTAs and Pt-BiOBr/TNTAs

Relative BET surface area was measured and calculated using our previously reported self-designed method[8,9], as listed in Tab.1. The relative BET surface areas of Pt/TNTAs, BiOBr/TNTAs and Pt-BiOBr/TNTAs are much larger than that of bare TNTAs, and Pt-BiOBr/TNTAs has the highest relative BET surface area. This implies that loading appropriate amounts of tiny Pt NPs and BiOBr NFs on the walls of TiO_2NTs may remarkably increase the specific surface area of the bare TNTAs. As a consequence, Pt-BiOBr/TNTAs may display superior PC activity due to its capacity to enhance the light absorption, increase the contact area between adsorbed dye molecules and the catalyst, and improve the molecule transport of reactants and products.

Tab.1 Relative BET surface areas of Ti foil and the as-prepared bare TNTAs, Pt/TNTAs, Pt-BiOBr/TNTAs and BiOBr/TNTAs

Samples	Relative BET specific surface area (m^2/cm^2)
Ti foil	2.531×10^{-4}
Bare TNTAs	0.273 2
Pt/TNTAs	0.334 6
Pt-BiOBr/TNTAs	0.587 4
BiOBr/TNTAs	0.473 5

PC activity and stability of the as-prepared samples were evaluated by degradation of MO solution under visible-light irradiation, as shown in Fig.8(a). Owing to the intrinsic wide bandgap of TiO_2, bare TNTAs show negligible PC activity under visible-light irradiation. In contrast, Pt/TNTAs, BiOBr/TNTAs and Pt-BiOBr/TNTAs exhibit obvious visible-light PC activities, and especially Pt-BiOBr/TNTAs show the best PC activity. After 180 min of PC degradation, the removal ratio of MO over Pt-BiOBr/TNTAs reaches 88.9%, while the removal ratios of MO over Pt/TNTAs, BiOBr/TNTAs are only 25.2% and 38.9%, respectively.

In addition, the reusability and long-term stability of Pt-BiOBr/TNTAs were further evaluated by the cycling tests and after ten days in the PC degradation of MO under visible-light irradiation, as shown in Fig.8(c) and (d). The PC efficiency remains stable after 4 cycles and even 10 days later. What is more, as the FESEM image and the XRD patterns shown in Fig.9(a) and (b), no obvious changes in the morphology and phase structure can be observed after the PC degradation 10 days later. According to all above analyses, it can be concluded that compared with Pt/TNTAs and BiOBr/TNTA, the multi-heterostructured Pt-BiOBr/TNTAs exhibit remarkably enhanced visible-light PC activity as well as favourable reusability, long-term stability towards the degradation of organic pollutants.

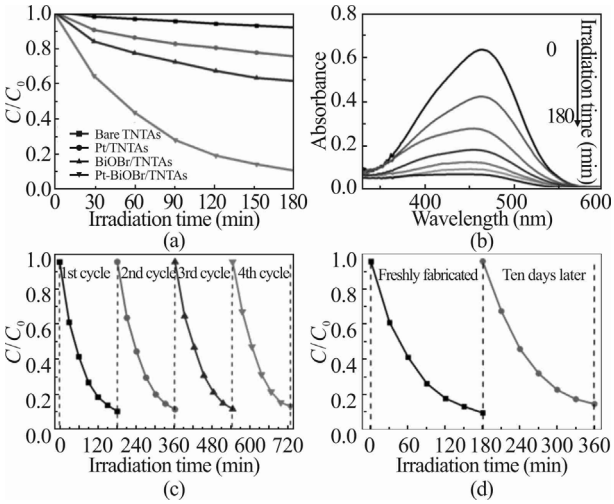

Fig.8 (a) PC activities of bare TNTAs bare TNTAs, Pt/TNTAs, BiOBr/TNTAs and Pt-BiOBr/TNTAs under visible-light irradiation; (b)UV-visible absorbance spectra of MO degraded using Pt-BiOBr/TNTAs as catalyst; Cycling degradation curves of Pt-BiOBr/TNTAs for (c) 4 cycles and (d) ten days later

As is well known, the PC degradation process is mainly based on the reaction between the photo-generated carriers and the adsorbed reactants on the surface of the semiconductor catalyst. However, the photo-generated electrons and holes can easily recombine during the process of migration to the catalyst surface. Therefore, to figure out how the deposited Pt NPs and BiOBr NFs affect the generation and separation of photo-generated carriers as well as the effective adsorption of reactants will help to reveal the essence of remarkably enhanced PC performance of Pt-BiOBr/TNTAs, Fig.10 shows the schematic diagram for the energy band structure as well as the possible charge separation mechanism for multi-heterostructured Pt-BiOBr/TNTAs under visible-light excitation.

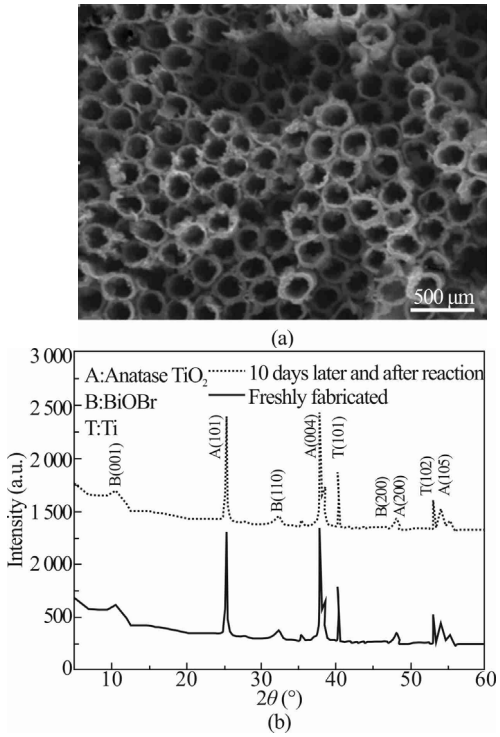

Fig.9 Characterization results of Pt-BiOBr/TNTAs after the PC degradation of MO solution 10 days later, including (a) FESEM image as well as (b) the XRD patterns before and after degradation reaction

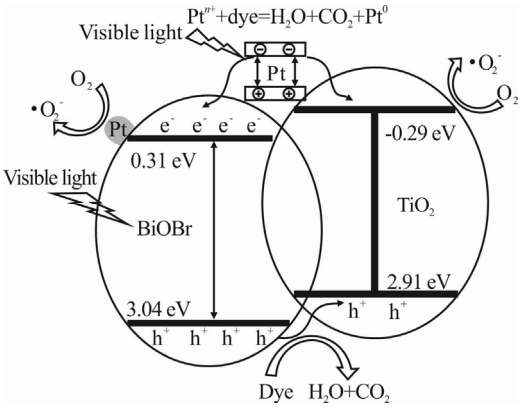

Fig.10 Schematic diagram for energy band as well as the possible charge separation and transfer mechanism under visible-light irradiation for multi-heterostructured Pt-BiOBr/TNTAs

BiOBr with a narrow band gap of 2.73 eV can absorb visible light for the generation of photo-generated electrons (e^-) and holes (h^+), while anatase TiO_2 can not be excited due to its intrinsic wide band gap of 3.20 eV. At the heterojunction of BiOBr/TiO_2, owing to the higher valence band (VB) position of BiOBr (3.04 eV) compared with that of TiO_2 (2.91 eV), photo-generated holes in the VB of BiOBr can transfer to that of TiO_2, and the holes in the VB of both TiO_2 and BiOBr may react directly with dye molecules. Such a carrier transfer is known as the Fermi level alignment if the material can be described by Fermi-Dirac distribution[18]. Besides, the deposited Pt NPs can as well absorb visible light and generate photoelectrons and Pt^{n+} due to the LSPR effect. At the heterojunction of Pt/TiO_2 and Pt/BiOBr, the LSPR-induced electrons with higher energy level diffuse into the conduction band (CB) of BiOBr or TiO_2, and then are trapped by surface absorbed O_2 to form superoxide ions ($\cdot O_2^-$) and other reactive oxygen species, while the Pt^{n+} may react with dye molecules directly to generate inorganic small molecules. On the other hand, Pt NPs can act as electron traps to promote the electron-hole separation as well, and the trapped electrons can be withdrawn by the absorbed O_2 on the surface of BiOBr[6,19,20]. Based on above analysis, it is clear that the yield of photo-generated electron-hole pairs can be remarkably enhanced due to the effective visible-light absorption by BiOBr and Pt, and meanwhile photo-generated electrons and holes can be effectively separated by multiple heterojunction formed among Pt, BiOBr and TiO_2.

Moreover, after co-modifying TNTAs with Pt NPs and BiOBr NFs, the microstructure characteristics, such as open tube-mouth, certain intertube spacings and rough surface, are facile for light injection and absorption as well as efficient mass transport. Furthermore, significant increase in the specific surface area also helps to enhance light absorption, increase the effective contact area between the absorbed dye molecules and catalyst, and benefit the molecule transport of reactants or products.

According to above discussion, strong visible-light absorption by the loaded Pt NPs and BiOBr NFs, lower recombination rate of photo-generated electrons and holes by the multiple heterojunction, microstructure characteristics and larger specific surface area are together responsible for the remarkably enhanced PC performance of Pt-BiOBr/TNTAs.

Novel multi-heterostructured Pt-BiOBr/TNTAs catalyst is firstly achieved by surface co-modifying ordered and spaced TiO_2 NTs with both Pt NPs and BiOBr NFs using anodization followed by solvothermal and S-CBD method. Thanks to the strong visible-light absorption by the deposited Pt NPs and BiOBr NFs, lower recombination rate of photo-generated electrons and holes attributes to the multiple heterojunction, microstructures for facile light injection and adsorption as well as efficient mass transport, and larger specific surface area for enhancing light absorption, increasing the effective contact area between the absorbed molecules and catalyst and benefiting the molecule transport of reactants or products. The as-fabricated Pt-BiOBr/TNTAs exhibit remarkable visible-light PC activity and favourable stability towards the degradation of organic pollutants.

References

[1] J. Bai and B. X. Zhou, Chemical Reviews **114**, 10131 (2014).

[2] C. A. Grimes, Journal of Materials Chemistry **17**, 1451 (2007).
[3] A. E. R. Mohamed and S. Rohani, Energy & Environmental Science **4**, 1065 (2011).
[4] B. L. Xu, C. X. Liu, H. Y. Sun and Y. R. Zhong, Optoelectronics Letters **10**, 84 (2014).
[5] S. G. Kumar and L. G. Devi, Journal of Physical Chemistry A **115**, 13211 (2011).
[6] K. L. Zhang, C. M. Liu, F. Q. Huang, C. Zheng and W. D. Wang, Applied Catalysis B: Environmental **68**, 125 (2006).
[7] H. F. Cheng, B. B. Huang and Y. Dai, Nanoscale **6**, 2009 (2014).
[8] J. J. Hu, J. Q. Liu, L. L. Ruan, H. D. Bian, X. Y. Zhang and Y. C. Wu, Optoelectronics Letters **11**, 5 (2015).
[9] J. Q. Liu, L. L.Ruan, S. B. Adeloju and Y. C. Wu, Dalton Transactions **43**, 1706 (2014).
[10] L. L. Ruan, J. Q. Liu, Q. Zhou, J. J. Hu, G. Q. Xu, X. Shu and Y. C. Wu, New Journal of Chemistry **38**, 2506 (2014).
[11] H. F. Cheng, B. B. Huang, P. Wang, Z. Y. Wang, Z. Z. Lou, J. P. Wang, X. Y. Qin, X. Y. Zhang and Y. Dai, Chemical Communications **47**, 7054 (2011).
[12] M. S. P. Francisco, V. R. Mastelaro, P. A. P. Nascente and A. O. Florentino, Journal of Physical Chemistry B **105**, 10515 (2001).
[13] K. Siuzdak, M. Szkoda, M. Sawczaka and A. Lisowska-Oleksiakb, New Journal of Chemistry **39**, 2741 (2015).
[14] X. L. Tan, Q. H. Fan, X. K. Wang and B. Grambow, Environmental Science & Technology **43**, 3115 (2009).
[15] Z. K. Zheng, B. B. Huang, X. Y. Qin, X. Y. Zhang, Y. Dai and M. H. Whangbo, Journal of Materials Chemistry **21**, 9079 (2011).
[16] J. X. Xia, S. Yin, H. M. Li, H. Xu, L. Xu and Y. G. Xu, Dalton Transactions **40**, 5249 (2011).
[17] H. D. Bian, X. Shu, J. F. Zhang, B. Yuan, Y. Wang, L. J. Liu, G. Q. Xu, Z. Chen and Y. C Wu, Chemistry-An Asian Journal **8**, 2746 (2013).
[18] A Tanaka, K Hashimoto and H. Kominami, Journal of the American Chemical Society **136**, 586 (2014).
[19] Y. L. Lee and Y. S. Lo, Advanced Functional Materials **19**, 604 (2009).
[20] C. L. Yu, F. F. Cao, G. Li, R. F. Wei, J. C. Yu, R. C. Jin, Q. Z. Fan and C. Y. Wang, Separation and Purification Technology **120**, 110 (2013).